

Supporting Information for

Impact Resistance of Nanocellulose Films with Bioinspired Bouligand Microstructures

Xin Qin, Benjamin Marchi, Zhaoxu Meng, Sinan Keten*

Department of Civil and Environmental Engineering and Department of Mechanical Engineering, Northwestern
University, 2145 Sheridan Road, Evanston, IL, 60208

*Corresponding Author: s-keten@northwestern.edu

Details of mesoscopic modeling approach

The bead-spring mesoscopic model used for cellulose nanocrystals (CNCs) is representative of cellulose I with the I β crystal structure. This particular cellulose structure was considered given its abundance in nature and extensive experimental and computational characterization.¹⁻² In this model, CNCs with exposing (110) surfaces, consisting of a 36-chain structure (cross-section: 3.57 nm by 3.38 nm), were mapped to coarse-grained (CG) beads, consistent with experimental observations.³⁻⁴ The CG bead radius was set at $R = 17 \text{ \AA}$, representing 3 repeat-units of atoms (4536 total atoms, 10.38 \AA in length) along the axial direction. The equilibrium bond length was $b_0 = 31.14 \text{ \AA}$, per the geometry, and the mass for the CG bead was approximately 35000 g/mol. The crystals employed in simulations are approximately 1 micron long, which are similar to the dimensions of CNCs found in tunicates.¹

All-atomistic molecular dynamics (MD) mechanical characterization simulations, including uniaxial tensile, 3-point bending, and adhesion energy calculations, were carried out to

parameterize the CG force fields under a strain energy conservation paradigm. The NAMD molecular dynamics package⁵ and the CHARMM⁶ force field were used in the all-atomic simulations, with full electrostatics calculated through the particle mesh ewald (PME) method and a simulation timestep of 1 fs. All the CG-MD simulations were conducted using LAMMPS and visualizations were done using VMD.⁷⁻⁸ All simulations were performed at room temperature (300K) unless otherwise stated. The uniaxial tensile tests, 3-point bending tests, and adhesion energy calculations were used to determine bond parameters, angle terms, and nonbonded interactions, respectively. Complete details, including specific CG model parameters and validation, can be found in previous work,⁹ and the functional forms and parameters are listed below in Table S1.

Table S1. Functional forms and parameters of the CG model force field for CNC

Interaction	Function Form	Parameters
Bond	$V_{bond} = k_b(b - b_0)^2$ for $b < b_{cut}$	$b_0 = 31.14 \text{ \AA}$ $k_b = 260 \text{ kcal} \cdot \text{mol}^{-1} \cdot \text{\AA}^{-2}$ $b_{cut} = 32.7 \text{ \AA}$
Angle	$V_{angle} = k_\theta(\theta - \theta_0)^2$	$\theta_0 = 180^\circ$ $k_\theta = 76000 \text{ kcal} \cdot \text{mol}^{-1} \cdot \text{rad}^{-2}$
Nonbonded	$V_{nb} = D_0 \left[e^{-2\alpha(r-r_0)} - 2e^{-\alpha(r-r_0)} \right]$ for $r < r_{cut}$	$r_0 = 36 \text{ \AA}$ $D_0 = 240 \text{ kcal} \cdot \text{mol}^{-1}$ $\alpha = 0.3 \text{ \AA}^{-1}$ $r_{cut} = 60 \text{ \AA}$

Sensitivity of projectile nonbonded potential on impact response

The sensitivity of the nonbonded potential between the projectile and film on the impact response was explored. For the range of the Lennard Jones well depth for the projectile-film

interaction, ϵ_{pf} , examined herein ($0.1 < \epsilon_{pf} < 1000$ kcal/mol), the magnitude of the potential was found to minimally affect the predicted dynamic response (Figures S1a-b). With increasing ϵ_{pf} , the noise in the projectile force history increased; however, the mean force response during the primary impact event remained approximately constant. At large initial velocities, high ϵ_{pf} (> 500 kcal/mol) values corresponded to higher projectile reaction forces during the penetration process as the projectile lost velocity (Figure S1b). This can be attributed to increased friction between the projectile and the film.

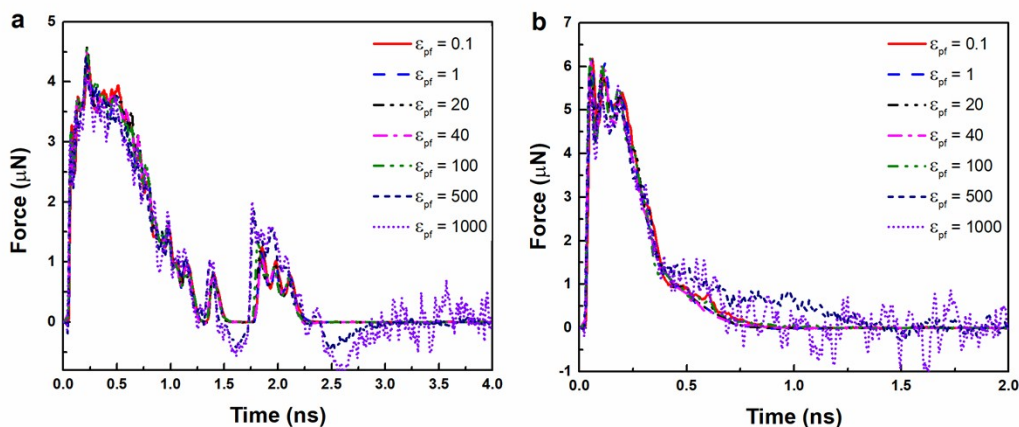


Figure S1: Force histories of a representative Bouligand film ($\gamma = 36^\circ$) for variable nonbonded interactions ϵ_{pf} with (a) $V_0 = 200$ m/s and (b) $V_0 = 450$ m/s.

Structure deformation and damage

To further analyze the structural response during impact, impact simulations with relatively low initial velocity ($V_0 = 250$ m/s, a velocity below every V_{50}) were conducted to quantify the number of bonds broken during the impact event. As shown in Figure S2, Bouligand films with a relatively large number of bonds broken at velocities well below V_{50} correlated with inferior impact resistance (Figure 2). The significance of this correlation was examined using a

linear regression, which showed a strong linear relationship between V_{50}/ρ and the number of bonds broken ($P_{slope} < 0.001$). This means that structural integrity is likely an important feature of Bouligand microstructures with high impact tolerance.

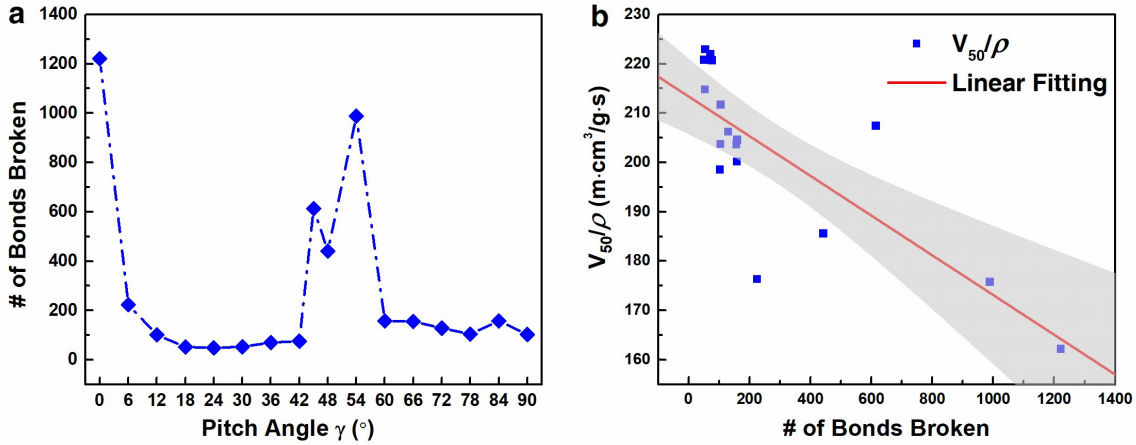


Figure S2: (a) Relationship between pitch angle and number of bonds broken, and (b) linear relationship between V_{50}/ρ and number of bonds broken. The red line corresponds to the best fit linear model and the filled area is the 95% mean confidence interval.

Quasi-static nanoindentation analysis

To identify any material property contributions to impact resistance, nanoindentation simulations were carried out on each of the Bouligand films. The nanoindentation simulations followed the same minimization and equilibration procedure as the ballistic tests. After equilibration, the Bouligand films were indented by a spherical indenter with a radius of 80 nm at their geometric center and a constant rate of 1 m/s. A purely repulsive, harmonic interaction was assumed between the indenter and the CNC films, represented by $F(r) = -K(r - R)^2$, where K is the force constant ($5000 \text{ kcal/mol}\cdot\text{\AA}^3$), r is the distance from an atom to the center of the indenter with a radius of R . The indenter was treated as rigid and the magnitude of the harmonic

potential had minimal influence on the observed behavior; indenter force and indentation depth were monitored during the simulations. The peak force and nanoindentation work done until the peak force was reached were extracted during the simulations. Five independent simulations were conducted for each structure. Linear regression analyses failed to provide sufficient evidence ($P_{slope} > 0.05$) to reject the null hypotheses of nonzero relationships between quasi-static film material properties and ballistic performance (Figure S3).

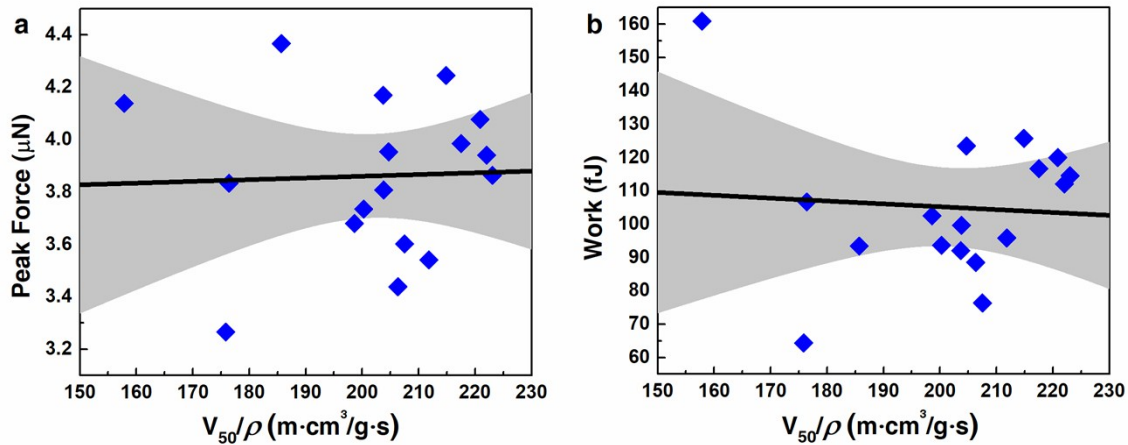


Figure S3: Relationship between (a) peak force and (b) work and specific ballistic velocity. The black lines are the linear regressions and the gray shaded area are the corresponding 95% mean confidence intervals.

Interlayer interactions for different Bouligand microstructures

To show the influence of pitch angles on the interlayer interactions, nonbonded pairwise interactions between adjacent layers were calculated through direct summation for each Bouligand structure. The average interlayer energy is plotted against pitch angle in Figure S4. These data support that Bouligand microstructures with pitch angles in the optimal performance range tend to have smaller interactions (Figure 5c).

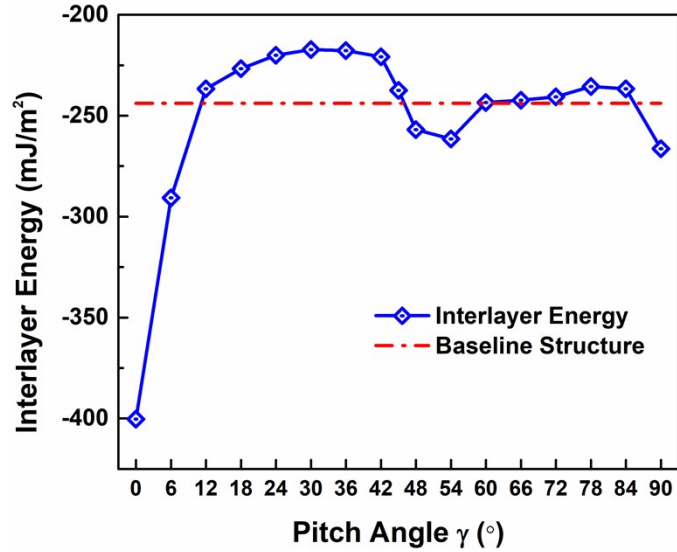


Figure S4: Relationship between interlayer energy and pitch angle.

Crack twisting in Bouligand film

Experimental and theoretical investigations have shown that crack twisting is an important mechanism for Bouligand structures to enhance their impact resistance.¹⁰⁻¹² This crack twisting phenomenon was readily apparent during penetrating impacts of certain Bouligand films (Figure S5). Crack twisting between different layers greatly increases crack path lengths and surface areas through the thickness of films. This reduces the strain energy release rate to enhance ballistic performance. Smaller interlayer interactions (Figure S4) further contribute to crack twisting via increased interlayer openings and improved crack deflection, leading to superior impact resistance.

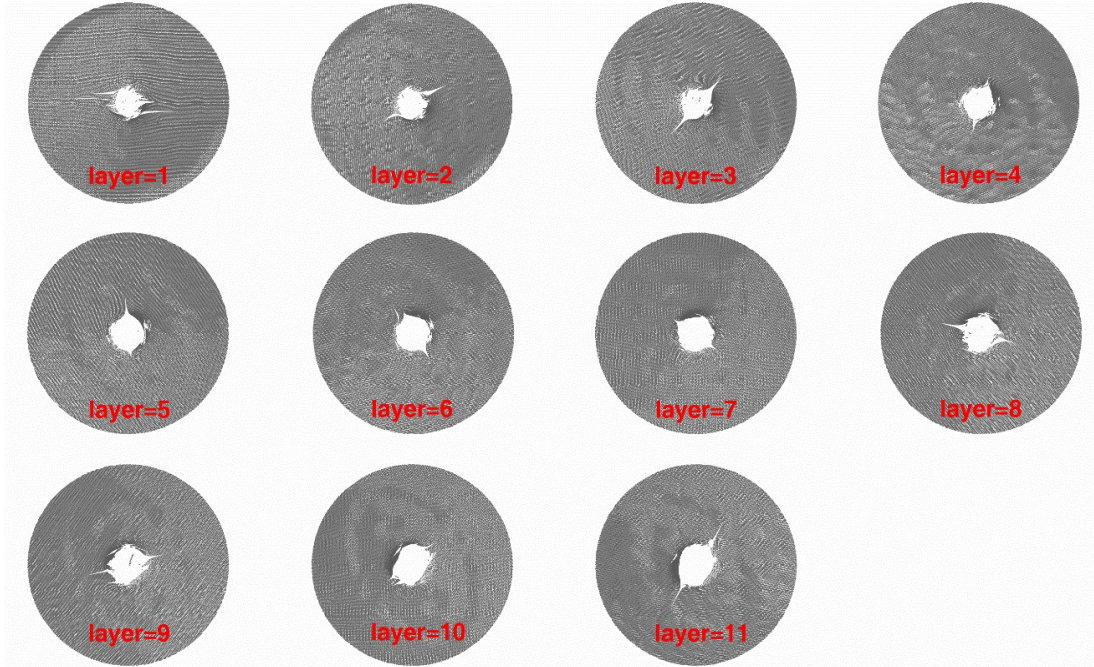


Figure S5: Top views of different layers ($\gamma=24^\circ$) showing the crack twisting of Bouligand microstructures during impact.

Splitting failure in Bouligand films

For Bouligand microstructures with very small pitch angles ($< 6^\circ$), CNC films tend to fail by fiber splitting, as only the fibers directly under the projectile support the impact and there lacks effective force and energy transfer mechanisms within the films. Figure S6 shows snapshots of aligned, unidirectional ($\gamma=0^\circ$) CNC film failure with splitting.



Figure S6: Splitting failure for Bouligand film with $\gamma=0^\circ$: (a) top view and (b) side view of the first layer, and (c) side view of the entire structure splitting. Different colors represent individual CNC fibers and the grey spheres are the projectiles.

Effect of interfacial properties on failure mechanisms in Bouligand films

The strength of nonbonded, interfiber interactions also affect the failure mechanisms exhibited by CNC Bouligand thin films. For the most part, as the strength of the nonbonded interaction increases (increasing D_0), so too does the number of intra-CNC bonds broken (Fig. S7). That being said, the interplay between D_0 and holistic film failure is complex and not well captured by a single metric like the number of bonds broken. The amount of interlayer sliding is also dictated by the strength of the nonbonded interaction, with higher D_0 leading to less sliding, higher effective interlayer shear stiffness, and less local fiber fragmentation (Fig. S8). These factors combine to facilitate premature projectile penetration and reduced ballistic resistance (Fig. 5a).

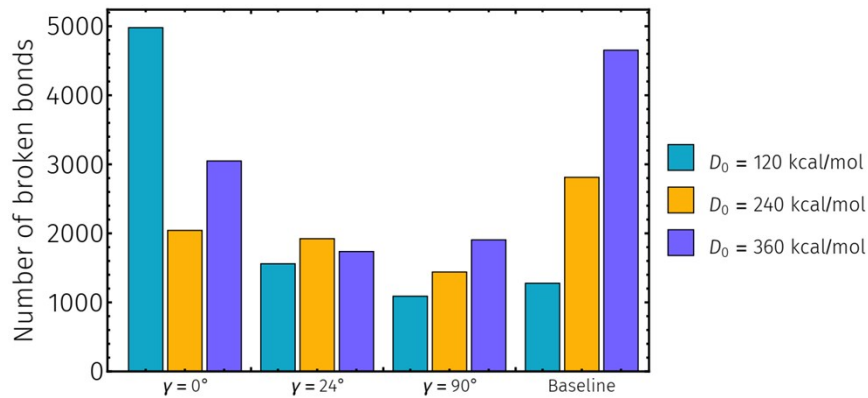


Figure S7: Effect of interfacial adhesion energy (D_0) on the total number of bonds broken with $V_0 = 400$ m/s.

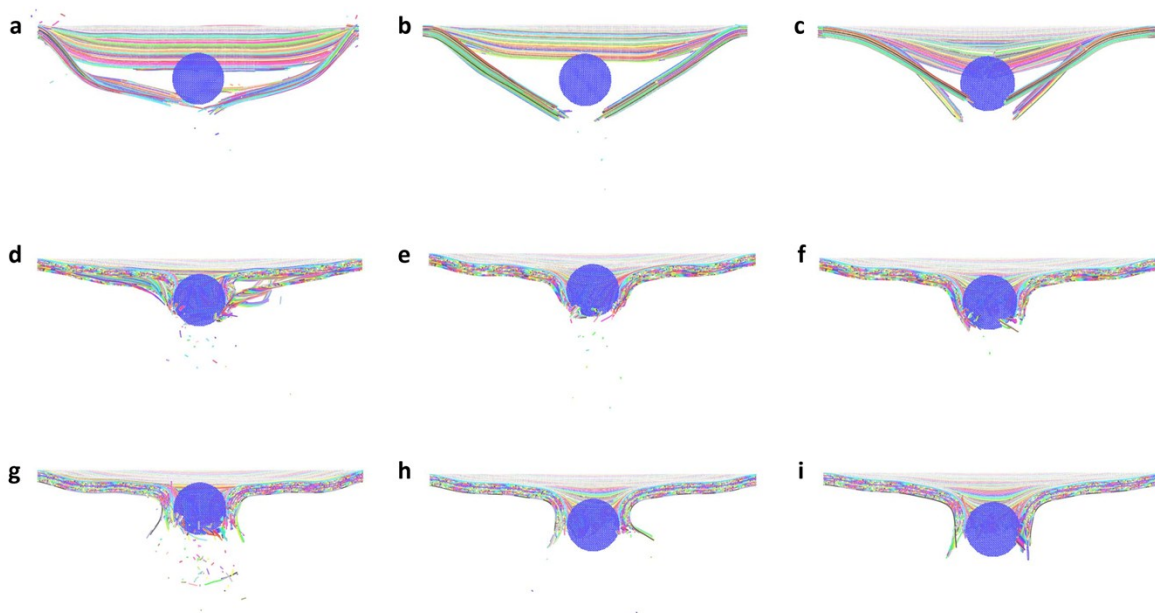


Figure S8: Side views of film failures for (a-c) $\gamma = 0^\circ$, (d-f) $\gamma = 24^\circ$, and (g-i) quasi-isotropic baseline structures with various interfacial strengths ((a,d,g) $D_0 = 120$ kcal/mol; (b,e,h) $D_0 = 240$ kcal/mol; (c,f,i) $D_0 = 360$ kcal/mol) subjected to projectile impacts with $V_0 = 400$ m/s. Different colors chains represent individual CNC fibers and the blue spheres are the projectiles.

References

- (1) Moon, R. J.; Martini, A.; Nairn, J.; Simonsen, J.; Youngblood, J. Cellulose Nanomaterials Review: Structure, Properties and Nanocomposites. *Chem. Soc. Rev.* **2011**, *40* (7), 3941-94.
- (2) Sinko, R.; Qin, X.; Keten, S. Interfacial Mechanics of Cellulose Nanocrystals. *MRS Bull.* **2015**, *40* (04), 340-348.
- (3) Elazzouzi-Hafraoui, S.; Nishiyama, Y.; Putaux, J.-L.; Heux, L.; Dubreuil, F.; Rochas, C. The Shape and Size Distribution of Crystalline Nanoparticles Prepared by Acid Hydrolysis of Native Cellulose. *Biomacromolecules* **2008**, *9* (1), 57-65.
- (4) Mtibe, A.; Linganiso, L. Z.; Mathew, A. P.; Oksman, K.; John, M. J.; Anandjiwala, R. D. A Comparative Study on Properties of Micro and Nanopapers Produced from Cellulose and Cellulose Nanofibres. *Carbohydr. Polym.* **2015**, *118*, 1-8.
- (5) Phillips, J. C.; Braun, R.; Wang, W.; Gumbart, J.; Tajkhorshid, E.; Villa, E.; Chipot, C.; Skeel, R. D.; Kalé, L.; Schulten, K. Scalable Molecular Dynamics with Namd. *J. Comput. Chem.* **2005**, *26* (16), 1781-1802.
- (6) Brooks, B. R.; Brooks, C. L.; Mackerell, A. D.; Nilsson, L.; Petrella, R. J.; Roux, B.; Won, Y.; Archontis, G.; Bartels, C.; Boresch, S.; Cafflich, A.; Caves, L.; Cui, Q.; Dinner, A. R.; Feig, M.; Fischer, S.; Gao, J.; Hodoscek, M.; Im, W.; Kuczera, K.; Lazaridis, T.; Ma, J.; Ovchinnikov, V.; Paci, E.; Pastor, R. W.; Post, C. B.; Pu, J. Z.; Schaefer, M.; Tidor, B.; Venable, R. M.; Woodcock, H. L.; Wu, X.; Yang, W.; York, D. M.; Karplus, M. Charrm: The Biomolecular Simulation Program. *J. Comput. Chem.* **2009**, *30* (10), 1545-1614.
- (7) Humphrey, W.; Dalke, A.; Schulten, K. Vmd: Visual Molecular Dynamics. *J. Mol. Graphics* **1996**, *14* (1), 33-38.

- (8) Plimpton, S. Fast Parallel Algorithms for Short-Range Molecular Dynamics. *J. Comput. Phys.* **1995**, *117* (1), 1-19.
- (9) Qin, X.; Feng, S.; Meng, Z.; Keten, S. Optimizing the Mechanical Properties of Cellulose Nanopaper through Surface Energy and Critical Length Scale Considerations. *Cellulose* **2017**.
- (10) Fischer, F. D.; Kolednik, O.; Predan, J.; Razi, H.; Fratzl, P. Crack Driving Force in Twisted Plywood Structures. *Acta Biomater.* **2017**, *55*, 349-359.
- (11) Nikolov, S.; Petrov, M.; Lymperakis, L.; Friák, M.; Sachs, C.; Fabritius, H.-O.; Raabe, D.; Neugebauer, J. Revealing the Design Principles of High-Performance Biological Composites Using Ab Initio and Multiscale Simulations: The Example of Lobster Cuticle. *Adv. Mater.* **2010**, *22* (4), 519-526.
- (12) Suksangpanya, N.; Yaraghi, N. A.; Kisailus, D.; Zavattieri, P. Twisting Cracks in Bouligand Structures. *J. Mech. Behav. Biomed. Mater.* **2017**.